HHS Public Access

Author manuscript

*Dev Cell*. Author manuscript; available in PMC 2017 March 21.

Published in final edited form as:

*Dev Cell*. 2016 March 21; 36(6): 668–680. doi:10.1016/j.devcel.2016.02.017.

# Multicolor Cell Barcoding Technology for Long-Term Surveillance of Epithelial Regeneration In Zebrafish

**Chen-Hui Chen**[1], **Alberto Puliafito**[2], **Ben D. Cox**[1], **Luca Primo**[2,3], **Yi Fang**[1], **Stefano Di Talia**[1], and **Kenneth D. Poss**[1]

[1]Department of Cell Biology, Duke University Medical Center, Durham, NC, 27710, USA

[2]Laboratory of Cell Migration, Candiolo Cancer Institute – FPO, IRCCS, Candiolo, Torino 10060, Italy

[3]Department of Oncology, University of Torino, Torino, 10060, Italy

## SUMMARY

Current fate mapping and imaging platforms are limited in their ability to capture dynamic behaviors of epithelial cells. To deconstruct regenerating adult epithelial tissue at single-cell resolution, we created a multicolor system, *skinbow*, that bar-codes the superficial epithelial cell (SEC) population of zebrafish skin with dozens of distinguishable tags. With image analysis to directly segment and simultaneously track hundreds of SECs in vivo over entire surface lifetimes, we readily quantified the orchestration of cell emergence, growth, repositioning, and loss under homeostatic conditions and after exfoliation or appendage amputation. We employed *skinbow*-based imaging in conjunction with a live reporter of epithelial stem cell cycle activity, and as an instrument to evaluate the effects of reactive oxygen species on SEC behavior during epithelial regeneration. Our findings introduce a platform for large-scale, quantitative in vivo imaging of regenerating skin and reveal unanticipated collective dynamism in epithelial cell size, mobility, and interactions.

## Graphical Abstract

Contact: kenneth.poss@duke.edu; phone 919-684-8457; fax 919-684-8090.

SUPPLEMENTAL INFORMATION

Supplemental Information including 7 figures and 7 movies and can be found with this article online.

**AUTHOR CONTRIBUTIONS**

C.C. and K.D.P. designed the experimental strategy, analyzed data, and prepared the manuscript. C.C. generated transgenic zebrafish and performed regeneration experiments and imaging. A.P. and S.D. designed and performed quantitative analyses. B.C., Y.F., and L.P. contributed transgenic zebrafish or analysis support. All authors made contributions to the manuscript.

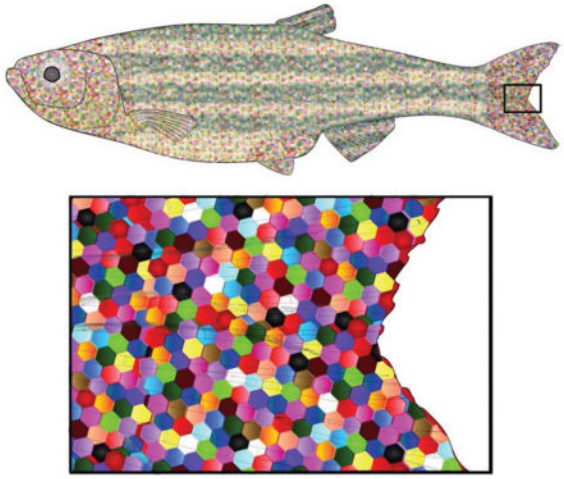

***skinbow*: A platform for live imaging and quantitative analysis of epithelial regeneration**

## INTRODUCTION

Skin provides a multi-layered barrier between the environment and interior tissues, and undergoes regular cycles of cell loss and replacement. Within a stratified epithelium, superficial and suprabasal cells generally do not undergo cell division, but instead are maintained by differentiation from a pool of stem cells in the underlying basal layer. Asymmetric division of these stem cells generates differentiated progeny that progressively displace toward the surface. Continued homeostatic maintenance by stem cells results in complete turnover of mammalian skin every few weeks. It is thought that positioning progenitor activity away from the surface is a general protective strategy for exposed tissue (Blanpain and Fuchs, 2009).

Major strides have been achieved in our understanding of the cellular bases of epithelial morphogenesis and regeneration in skin, its appendages (e.g. hair follicles), and more generally in epithelial structures like small intestinal villi. Advances have largely emerged from technologies to genetically label stem cells and then assess the spatiotemporal dynamics of their division and differentiation. These types of analyses hinge on the faithfulness of regulatory sequences to engage the initial lineage trace in a specific cell type, and the ability to assign progenitor-progeny relationships from fixed tissue specimens (Blanpain and Fuchs, 2014; Clevers, 2013; Macara et al., 2014; Watt, 2014). Conditions for rare labeling events can enable interpretation of clonal expansion from single progenitor cells, and biological explanation of data from these experiments can be aided by mathematical analysis and modeling. These studies have generated striking inferences; for instance, the observation that stem cell contributions tend to drift toward clonality during the rapid turnover of intestinal epithelia (Barker et al., 2007; Griffiths et al., 1988; Snippert et al., 2010; Winton and Ponder, 1990). Because these experiments are retrospective in nature, they do not capture the dynamism of cells under investigation, and thus intricate or transient cell activities like size and shape changes, division planes, motility, cell-cell interactions, or collective behaviors require some level of speculation.

Recent, pioneering live imaging experiments using intravital multiphoton microscopes have captured the developmental activities of stem cells in hair follicles and intestinal crypts over hours and days, identifying fundamental properties of stem cells (Ritsma et al., 2014; Rompolas et al., 2012; Rompolas et al., 2013). For instance, live imaging combined with clonal analysis in hair follicles or intestinal crypts revealed that position within the respective niche compartments influences the developmental decisions and relative contributions by individual stem cells (Ritsma et al., 2014; Rompolas et al., 2013). However, due to limitations of monochromic tagging and imaging platforms, only one or a small number of fluorescently labeled stem cells and their progeny are directly observed during each detection window. Thus, these in vivo approaches are not designed to identify and quantify large-scale population dynamics or collective behaviors of epithelial cells.

## DESIGN

Simultaneous tracking of most or all individual cells within a tissue compartment over long time periods would enable high-resolution quantification of transitory, dynamic, and collective activities of epithelial cells during homeostatic maintenance, as well as how these cell behaviors are modulated after injury or during disease. This challenging objective requires the capacity to unambiguously monitor most or all cells of a participating lineage in vivo in an adult tissue, distinguishing on the order of hundreds to thousands of cells within a seemingly homogeneous population. Among the required experimental components are: 1) an adult epithelial tissue compartment that is highly regenerative and can be easily accessed for live imaging experiments; 2) a system to stably label each individual cell within a large population with a distinct in vivo tag; and 3) cell tracking software for large-scale surveillance of individual cell dynamics over long periods of time.

In this study, we have developed a transgenic zebrafish line, *skinbow*, that incorporates Brainbow-based multicolor labeling to permanently barcode each superficial epithelial cell (SEC) in adult skin with one of several dozens of distinct colors. Through large-scale, in vivo imaging analysis of SEC populations covering zebrafish fins, we quantified individual and large-scale cell behaviors under homeostatic conditions, during repair of minor exfoliation injuries, and during regeneration of complex tissue after major amputation injuries. Our findings identify several unexpected collective cell responses and behaviors that are inherent to epithelial tissue regeneration in adult vertebrates.

## RESULTS

### Multicolor Labeling of Superficial Epithelial Cells

Fish epidermis is a simple stratified epithelium without keratinized layers, covered by transparent mucus (Rakers et al., 2013). This anatomy optimizes optical resolution of fluorescence imaging by reducing light scattering and absorption, obstacles that are often associated with deep tissue imaging (Figure 1A). Genetic fate-mapping has indicated that basal keratinocyte stem cells give rise to suprabasal cells and SECs in adult fish trunk and fin epidermis, the same positional hierarchy as in mammalian skin (Lee et al., 2014). In the process of establishing transgenic lines for Brainbow-based analysis (Gupta and Poss, 2012; Livet et al., 2007), we identified one line, *Tg(βact2:Brainbow1.0L/ubi:Tet3G/*

*TRE:CreER*$^{T2}$*)*$^{pd112}$ (referred to subsequently as *skinbow*; Figures 1B and S1A), with cell labeling that colors the entire body surface, including cornea, barbels, scales, and fins. The labeling is restricted to the superficial epithelial layer, and is not present in the suprabasal layer, basal layer, or underlying dermal tissues (Figures 1B–E and S1B; Movie S1). We defined these labeled cells as SECs because of their location. Migratory immune cells of this line are also labeled and detectable as a minor population in the epidermis (Figure S2B).

The *skinbow* DNA construct incorporates both tamoxifen- and tetracycline-inducible components, engineered for precise control of color recombination (Figure S1A). Despite this design, multicolor cell labeling occurred in *skinbow* SECs without addition of tetracycline or estrogen analogs, indicating selective leakiness in the system. *CreER* RNA was localized to superficial layers, and *β-actin2*-driven expression of Brainbow cassettes was restricted to differentiated *skinbow* SECs, likely a consequence of the transgene integration site (Figures S1C and S1D). Based on this specificity of expression and the imaging studies described below, we infer that SEC-specific recombination occurs transiently and selectively in SECs as they emerge on the body surface. By qPCR, we estimated the presence of over 100 copies of the 16 kb expression cassettes at a single integration site, and we reliably detected ~70 distinguishable hues in our imaging experiments (Figures 2A and 2B). This diversity consistently produced body surfaces with adjacent SECs of distinguishable colors.

## Live Imaging and Quantification of SEC Emergence, Size, Mobility, and Loss

We postulated that SEC-restricted expression and color diversity in *skinbow* animals would enable precise identification and tracking of individual SECs in a large field. To investigate the stability of surface fluorescence labeling in *skinbow* animals, we imaged a square 0.216 $mm^2$ area of the surface of each animal's caudal fin at 12-h intervals over 20 consecutive days by confocal microscopy. We imaged the identical area at each time, medial and just proximal to the fin cleft, in several animals (Figures 2A–2C). This 12-h interval was determined empirically to minimize phototoxicity while also obtaining necessary temporal resolution (Figures S3A–S3C), and image series alignment enabled SEC tracking from surface appearance to loss. More than 80% of SECs were labeled with a color distinct from all neighboring cells (Figures S2C and S2D), a hue that was stable on the fin surface as fluorescence intensity gradually increased with cell surface duration (Figures 2C, 2D, and Movie S2). This stability indicates that additional color recombination events were rare or absent in SECs once on the fin surface. To quantify size maturation over time in emergent SECs, we measured cell areas in full single cell trajectories, i.e. from appearance on the surface to loss. We found that emergent SECs acquire surface area rapidly at an average approximate rate of 50 $\mu m^2$/day until stabilizing at an average size of 287 $\mu m^2$ (Figure 2E; n = 186 trajectories). No SEC division events were observed throughout our imaging experiments, and cell migration within the organized epithelium, though detectable and quantifiable, was minimal (Figure 4D; n = 1146).

SEC loss was readily detectable and not associated with final cell size (Figures S3D and S3E; n = 186). By monitoring 186 SECs in 4 animals from cell appearance on the fin surface to loss, we calculated an average surface-span of 8.4 days (Figure 2F), with a range from 2

to 19.5 days. In these experiments, full (100%) replacement of SEC populations occurred within an average of 19.5 ± 0.9 days (n = 4 fish, 3626 events; Figure 2G). While the rate of cell replacement was consistent among animals and from day to day over the 20-day period (4.8% per day; n = 4), we cannot exclude possible effects of anesthesia and repetitive imaging on cell viability in these experiments. In humans, epithelial cell turnover has been indirectly assessed by monitoring the disappearance of fluorescent dye from skin surfaces, with studies indicating complete turnover over a very similar average period of 19.8 to 20.5 days in young adults (Grove and Kligman, 1983). Thus, the *skinbow* labeling and imaging platform we describe enables an extensive cataloging of lifetime events – "cell biographies" - for several hundreds of SECs within one imaging experiment.

## Mechanisms of SEC Homeostasis

Size maintenance in adult tissues can occur by matching cell loss and gain frequencies, and/or from compensatory size or shape changes by existing cells. In skin, epithelial cell replacement occurs through asymmetric division from proximate basal layer stem cells (Lechler and Fuchs, 2005), whereas in intestinal epithelium, cells shed at the villi tip are replaced by progeny of stem cells located at the crypt base (Barker et al., 2007). By visually inspecting individual SEC loss events, we identified two local responses. In the majority of cases (78.0%; n = 757), space vacated by a shed cell was rapidly filled by the rearrangement of neighboring cells and creation of new and stable (>48 h) cell-cell contacts (Figures 3A and 3D), a process taking just minutes (Figure S4). In the remaining 22.0% of cell loss events, a non-fluorescent and ostensibly unoccupied space was filled by a new SEC that gradually increased in size and fluorescence intensity over a period of days (Figures 3B and 3D).

A tendency to remodel local space after cell loss, versus in situ cell replacement, would rapidly reduce overall SEC number. However, SEC density was relatively stable over our imaging period (Figure S3B). Therefore, we suspected that de novo SEC creation was also occurring in areas without cell loss. From our imaging series, we identified and categorized individual cell gain events, detectable by a non-fluorescent opening between existing SECs that over a period of days becomes occupied by a fluorescent cell(s) (Figure 3C). We found that in 75.4% of cases (n = 839), SECs appearing in this manner are generated without a detectable neighbor cell loss event within the preceding or subsequent 12 h (Figures 3C and 3E). A smaller fraction of these events (24.6%) was concomitant with, preceded by, or followed by loss of at least one neighboring cell. Whereas these classes of gain events could be readily quantified, our imaging experiments detected but could not unambiguously categorize more sudden cell appearance events that occurred in relative proximity to cell loss or reorganization.

Cell loss and gain events did not distribute randomly in tissue regions. Measurement of the spatial distribution (L-Ripley's function) (Bailey and Gatrell, 1995; Ripley, 1977) of 3626 cell loss events indicated significantly larger clustering than expected for a random distribution of events (Figures 3F and 3G). The same quantification applied to 2500 cell gain events revealed an even higher degree of clustering (Figures 3F and 3H). This clustering suggests a causal relationship between loss and gain events, as does analysis indicating that

loss and gain events together occur preferentially in the same temporal window (within 48 h) and spatial location (within 2 cell radii) rather than randomly (Figure 3F). In sum, our experiments indicate that homeostatic SEC regeneration maintains equilibrium through at least 3 basic mechanisms: 1) new neighbor creation without cell addition; 2) *quid pro quo* cell birth; and 3) remote cell birth.

## Biphasic Regeneration of SECs after Minor Surface Injury

To visualize and quantify responses to physical trauma encountered either in the laboratory or natural environment, we gently exfoliated patches of SECs from *skinbow* fin surfaces, sparing underlying epithelial layers. We then immediately imaged animals, returned them to aquarium water, and performed time-lapse imaging over several days. Injuries exposed large areas of non-fluorescent epithelium (50–80% of surface area) that were quickly repopulated with SECs (Figure 4A and Movie S3). Color diversity allowed quantification of SEC motility by means of image correlation-based tracking algorithms. We monitored individual SECs spared by the injury during this period and identified two conspicuous behaviors. First, SECs showed a rapid, 65.7% increase in surface area within 12 hours post exfoliation (hpe), with many SECs expanding to twice as much surface area (Figures 4B and 4C; n = 55 from 3 animals). Most SECs returned to their approximate sizes at 2 hpe by 36 hpe (Figure 4C). Second, we found that many spared SECs rapidly migrated or were displaced into injured areas by 24 hpe (Figures 4A and 4D). This mobility revealed fluidity on the epithelial surface that was not manifested in the absence of injury (Figure 4D).

At 36 hpe, animals began recovering new SECs, and by 60 hpe they had regenerated ~80% of surface coverage on average (Figures 4E and 4F). For injuries that exposed ~80% of surface area, we measured an average of 17.9% of cell recovery per day, more than 3 times that of unperturbed homeostatic regeneration. The rate of regeneration in our experiments appeared to positively correlate with the extent of lost surface epithelium, an association that requires further examination but has been observed for zebrafish fins and salamander limbs regenerating from amputation injuries (Figure 4E) (Lee et al., 2005; Spallanzani and Maty, 1769). New SECs emerged quickly regardless of their positions with respect to spared SECs (Figures 4A and 4B), indicating that a pre-existing SEC scaffold is not critical for regeneration. Thus, SEC regeneration from exfoliation injury involves two distinct cell behaviors not evident in homeostatic SECs. First, spared cells in the injury site transiently increase surface area (referred to interchangeably as hypertrophy) and mobilize, temporarily reducing the area of exposed tissue. Second, a vigorous wave of regeneration replaces lost SECs *en masse*.

## Differential Tissue Deformation and Motility in Epithelial Sheets after Fin Amputation

Zebrafish fins are complex, bony appendages with marked regenerative capacity (Poss, 2010; Wehner and Weidinger, 2015). Within a few hours of fin amputation, the exposedstump tissue is quickly covered by epithelial cells. These initial events lead to formation of a multilayered wound epidermis that is capable of releasing signals important for new bone regeneration. We used *skinbow*, and additional transgenic reporter strains indicating specific fin cell types, to examine closure events by high-resolution time-lapse (2 min/frame) imaging in anaesthetized zebrafish. Unexpectedly, we observed frequent loss of

SECs at the amputation plane, with ~530 SECs shed per $mm^2$ area at 1 hour post amputation (hpa) (Figures 5A and 5B). We infer that these losses represent live cell loss events, or extrusion, as apoptosis typically requires 2 to 3 h (Elmore, 2007), and as these events are analogous to extrusion from overcrowding in the embryonic zebrafish epidermis (Eisenhoffer et al., 2012). Using a pan-epithelial line in combination with *skinbow* (Figure S5A), we found that the fin stump is rapidly covered first by basal and suprabasal cells, then closely trailed by SECs (Figure 5C). Amputation stumps were covered within 1 hpa in these experiments (Figure 5C and Movie S4). Thus, fin epithelial cells mobilize to heal injuries rapidly upon amputation injury, during which many SECs are shed upon closure.

While imaging wound closure, we detected regional differences in SEC behaviors. We monitored SECs by employing tracking algorithms and semi-automatic segmentation algorithms based on color differences, and then we quantified displacement and shape changes in individual cells (see Experimental Procedures for details). Interestingly, we found that after fin amputation, SECs mobilized in two distinct, alternating domains during wound healing, coinciding with regions overlying bony rays and soft tissue interray regions (Figures 5D and 5E; Movie S5). Interray SECs moved toward the amputation plane within minutes of amputation, whereas ray SECs displayed an associated but reduced response, with a velocity that was 40.3 μm/h lower than interray SECs (Figure 5F; n = 154 (interray) and 228 (ray) tracked SECs). Rates of movement were almost identical by 40 minutes post amputation (mpa), with a difference of only 3.5 μm/h (Figure 5F; SECs from the same animal are shown). Notably, some interray SECs near the amputation plane also moved laterally to close the wound (Figure 5D; indicated by white arrows).

To test the importance of mechanical coupling between these alternating sheets of SECs, we treated animals with gadolinium ($Gd^{3+}$), an inhibitor of stretch-activated ion channels, previously implicated in regulation of cell sheet forces (Hunter et al., 2014; Yang and Sachs, 1989). Notably, $Gd^{3+}$ treatment polarized the differences between movement velocities of interray and ray SEC sheets, indicating disrupted tissue interactions (Figure 5G and Movie S5). The effect of $Gd^{3+}$ treatment varied somewhat in magnitude among animals, but generally increased relative velocities of interray SEC movements (Figure 5H; n = 1657 (vehicle, 7 animals) vs. 1553 ($Gd^{3+}$, 5 animals) tracked SECs). The primary consequence was induction of even greater deformation rates in interray SECs between 40 and 10 mpa (18.1% greater (vehicle; n = 7 animals, 670 SECs) vs. 32.5% greater ($Gd^{3+}$; n = 5 animals, 462 SECs)), while at the same time reducing deformation rates in ray SECs (14.1% greater (vehicle, 602 SECs) vs. 4.3% greater ($Gd^{3+}$, 527 SECs)) (Figure 5I). Interestingly, amputated fins treated with $Gd^{3+}$ showed continued SEC displacement toward the amputation plane beyond 40 mpa mainly from interray SECs (Figure 5H), while failing to heal properly and allowing visible mesenchymal cell leakage (Figure S5B; Movie S6). Taken together, our findings indicate distinct deformation dynamics and velocity responses upon amputation in alternating sheets of SECs. Interray sheets (and/or their underlying epithelial layers) pilot events and possibly drag adjacent ray sheets over the exposed bony ray ends, interactions that occur with massive SEC extrusion at closure but help limit mesenchymal cell loss.

## Orchestration of Diverse SEC Behaviors during Fin Regeneration

Upon closure of amputation wounds, lost fin structures are replaced within two to three weeks, restoring the complex three-dimensional pattern of an appendage. As regeneration proceeds, new fin tissue is rapidly added to the stump, with both components requiring surface coverage with epithelial cells. The cellular strategy by which pre-existing cells assimilate with de novo pools in a rapidly growing tissue is a key, outstanding mechanistic question in vertebrate appendage regeneration.

After amputation surgeries and return to circulating aquarium water, we discovered that zebrafish fins shed large numbers of SECs near the amputation plane within the first 12 h (Figures 6A and S6A), likely due to the fragility of the wounded area. To assess the origins of SECs during fin regeneration, we tracked and quantified the behaviors of spared SECs, as well as the rate of new SEC creation, on *skinbow* fin surfaces from 12 to 96 hpa, a period of early osteogenic growth. By inferring transformation from corresponding points in images, we were able to reconstruct SEC movements from spared tissue and identify clear evidence for collective migration into regenerating tissue (Figures 6A and 6B). During the first 36 hours, SECs migrated past the amputation plane at greater velocities than the rate of distal tissue growth (8.2-fold at 12 hpa and 2.2-fold at 24 hpa), indicating active recruitment. After 36 hpa, these cells were displaced at rates indistinguishable from tissue growth (Figure 6C; representative dataset from one animal, n = 85 cells tracked). By 96 hpa, SECs had traveled 420 μm on average (n = 500 from 5 animals) into the regenerate from their origins proximal to the amputation plane (Figure 6D). Regenerating fins also acquired SECs by de novo creation (Figure 6A), and the extent of coverage from this mechanism gradually increased in the moving growth front as regeneration progressed (Figures 6E and S6B). By 48–60 hpa, the front of advancing tissue was nearly 50% covered, primarily from new SECs born on the surface of regenerates after 24 hpa, and full coverage was achieved by 10 dpa (87.6% (10 dpa) vs. 89.3% (uninjured), n = 5); Figures S7A and S7B). Interestingly, individual SECs at the distal tips of 10 dpa regenerates were enlarged, with 65% more cell surface area than more proximal SECs (n = 499 cells from 5 animals; Figures 6F–6H). Distal SEC hypertrophy was less prominent when sampled at 14 dpa (34% larger), and had essentially disappeared by 30 dpa (Figures 6H and 6I).

Thus, the construction of the surface epithelium of regenerating fin structures involves dynamic, sequential modulations of SEC mobility, new cell creation, and cell surface area. After fin amputation, mechanically coupled epithelial layers seal the wound in an alternating pattern that occurs with massive SEC extrusion. Next, the initial surface coverage involves rapid recruitment of spared SECs over long distances. During regenerative outgrowth, newly created SECs continue to integrate with pre-existing SECs, and de novo SECs become the predominant cellular supply of surface epithelium. Upon full coverage, actively regenerating fin portions retain a localized, hypertrophic SEC phenotype that resolves at completion of appendage replacement (Figure S7C).

## Reactive Oxygen Species Levels Control SEC Regeneration Dynamics

SECs ultimately derive from post-mitotic suprabasal cells, which are maintained by proliferation of an underlying basal layer of stem/progenitor cells (Doupe et al., 2012;

Mascre et al., 2012). To determine whether stem cell activity could be simultaneously monitored with SEC behaviors, we created a FUCCI-based sensor line (Sakaue-Sawano et al., 2008; Sugiyama et al., 2009), *Tg(krtt1c19e:Venus-hGeminin)*$^{pd81}$, that enables live monitoring of dividing basal cells. When crossed into the *skinbow* background, we could concurrently monitor both SEC and underlying basal cell populations by longitudinal confocal imaging (Figure 7A and Movie S7). Under homeostatic conditions, basal keratinocyte division was minimal (Figure 7B). By contrast, and consistent with previous BrdU incorporation experiments using fixed tissue (Poleo et al., 2001; Santos-Ruiz et al., 2002), we identified many cycling basal cells in vivo 4 days after fin amputation (Figure 7B; images were captured from interray areas proximal to the amputation plane). Following exfoliation injury, we discovered that the basal cell layer was mostly devoid of Venus-hGeminin through 48 hpe, indicating that extensive regeneration of SECs occurs primarily through differentiation without stem cell proliferation (Figure 7C).

Injury-induced ROS production in epithelial tissue has been shown to mediate recruitment of leukocytes (Niethammer et al., 2009), and to modulate regeneration after amputation injuries in *Xenopus* and zebrafish (Gauron et al., 2013; Love et al., 2013). Using a redox-sensitive fluorogenic probe to indirectly measure injury-induced ROS in vivo (Mugoni et al., 2014), we found that ROS levels rapidly increased in the fin epithelium within hours of exfoliation (Figure 7D). The fluorescence intensity reached a peak at 2 to 12 hpe, before gradually diminishing to background levels by 48 hpe (Figure 7E), kinetics that correlate with those of SEC regeneration (Figure 7C). To investigate the impact of ROS levels on SEC regeneration, we treated *skinbow* animals with commonly used antioxidant and oxidant agents that affect hydrogen peroxide levels. We found that VAS2870, a pan-NADPH oxidase (NOX) inhibitor that disrupts hydrogen peroxide production in vivo (Niethammer et al., 2009; ten Freyhaus et al., 2006), reduced SEC regeneration by 74% (Figures 7F and 7G). Conversely, direct supplementation of hydrogen peroxide increased SEC coverage by 90% (Figures 7F and 7G) and individual cell surface area by 94% (n = 718 (vehicle, 8 animals) vs. 527 ($H_2O_2$, 5 animals); Figure 7H) at 48 hpe. Together, these results provide evidence that exfoliation of epidermal surface induces a transient burst of ROS that promotes regeneration, at least in part by regulation of cell hypertrophy.

## DISCUSSION

Here, we created a new platform consisting of multicolor labeling, live imaging, and large-scale cell tracking software, to generate biographies of intricate in vivo behaviors from surface birth to loss among individual adult zebrafish skin cells.

Under homeostatic conditions, SECs have limited mobility and size changes in their ~8 day surface life cycle. We describe here multiple distinct mechanisms to maintain equilibrium, defined by the location and timing of new cell emergence with respect to a cell loss event. How replacement is instructed by cell loss is a fundamental question; based on in vitro studies of epithelial monolayers, mechanisms that populate the surface epithelium are governed by mechanical tension between neighboring cells (Guillot and Lecuit, 2013; Macara et al., 2014; Shraiman, 2005). In vivo, a stratified epithelium must incorporate cell-cell interactions, both in-plane and off-plane, and cell-substrate interactions into instructions.

We suspect that ratios of the 3 major forms of cell replacement we describe here – new neighbor creation, *quid pro quo* replacement, and *de novo* creation - will differ in representation in epithelia among various developmental stages, underlying tissue substrates, and species.

Through large-scale monitoring of SECs during tissue regeneration, we identified effects of injury and regeneration on cell behaviors. Following amputation, fin ray and interray epithelial sheet SECs display differential motility, likely impacted by different stiffness or adhesive properties in underlying substrates (Discher et al., 2005). Differential motility of two adjacent epithelial sheets could create a significant deformation of the tissue. However, our experiments suggest that mechanical coupling among cells has the effect of reducing such deformations, inducing more uniform movements across the tissue that enable wound healing. Upon healing, the growth front of regenerating fins maintains coverage with a low-density SEC layer, populated in part through a mechanism of collective migration of SECs. Based on exfoliation injury alone, we have observed that low-density conditions stimulate SECs to quickly increase surface area and mobility, while accelerating de novo SEC emergence. It is possible that the integration of mechanisms of recruitment by collective cell migration, *de novo* SEC generation, and SEC hypertrophy during regeneration of amputated fins is a regulated program that prevents insurgence of large mechanical stresses and aids growth.

In most previous studies, stem cell activity has been directly or retrospectively traced, whereas our tools here focus attention on the differentiated epithelial cell endpoint. Similar analyses of fin epithelial stem cells in a live imaging platform will be possible with appropriate new tools, alone or in combination with *skinbow* readouts. In fact, we demonstrate here that live reporters of cell cycle phases can be employed in stem cells and assessed alongside of the *skinbow* signature of their SEC progeny. In future modifications of our tools and procedures, multicolor clonal tracing of stem cells using established regulatory sequences could be imaged longitudinally over weeks and in response to injury, to quantify the spatiotemporal output of many single stem cells during homeostasis or in response to injury. While recent evidence indicates that epithelial stem cells are heterogeneous (Donati and Watt, 2015; Schepeler et al., 2014), large-scale quantitative analysis of dynamic contributions by different stem cells in regenerating tissues will provide new insights into stem cell behaviors, plasticity, and regulation. Live imaging systems like that introduced in our study, as with others (Ritsma et al., 2014; Rompolas et al., 2013), can be instructive not only for regeneration biology, but also to enable powerful quantitative studies of aging tissue or malignancies like basal cell carcinoma.

*skinbow* animals and the level of their analysis we show here can illuminate molecular mechanisms of epithelial regeneration. ROS have been implicated in tissue regeneration through effects on leukocytes recruitment, apoptosis, JNK activation, and cell proliferation (Gauron et al., 2013; Love et al., 2013). Our proof-of-principle experiments here indicate direct or indirect effects of ROS on SEC cell size and creation that are readily monitored and quantified in live regenerating tissue. Transgenic lines that enable real-time detection of specific ROS forms in the epidermis (Bilan et al., 2013), or sensitive reporters or tunable

activators of other signaling effectors, can be simultaneously imaged with *skinbow* to associate high-resolution cell behaviors with the local actions of specific molecular factors.

## LIMITATIONS

A limitation in our system is the gradual loss of fluorescence intensity during time-lapse imaging. However, we show that with 12 h imaging intervals, the labeling is sufficiently stable to track an entire cell population over a long time period. We also cannot exclude possible phototoxic effects of repetitive laser illumination on cell behaviors, although we did not observe defects in regeneration during this study. Additionally, the presence of *Cre/loxP* sequences in *skinbow* animals limits applications involving *loxP*-flanked sequences at other loci.

## EXPERIMENTAL PROCEDURES

### Animals

Adult zebrafish 3–8 months of age were used for most experiments. Animal density was maintained at 3–4 per liter in all experiments. For generating the *skinbow* transgenic line, a transgenic construct containing the following DNA elements: 1) A 3.5 kb *ubiquitin* promoter driving a new generation of Tet-on transcription factor (Tet3G from Clontech); 2) a Tet-on responsive element driving the recombinase CreERT2; and 3) a 5.8 kb β-*actin2* promoter driving the Brainbow 1.0 fluorescent protein cassette was assembled by yeast recombinational cloning. The entire construct was flanked with I-SceI sites to facilitate transgenesis. The full name of the *skinbow* line, in which the transgene is inherited as a single insertion site is *Tg(βact2:Brainbow1.0L/ubi:Tet3G/TRE:CreERT2)*$^{pd112}$. The *Tg(β-act2:EGFP)*$^{zp5}$ line was employed to visualize all fin epithelial cell layers (Traver et al., 2003). To generate *Tg (msxC:DsRed2)*$^{pd113}$ zebrafish, the translational start codon of *msxc* in the BAC clone DKEYP-85D1 was replaced with the *dsred2* cassette by Red/ET recombineering technology (Gene Bridges). The 5′ and 3′ homologous arms for recombination were about 300-base pair (bp) fragments upstream and downstream of the start codon, and were subcloned into a pBluescript vector to flank the *dsred2* cassette. To avoid aberrant recombination between the *dsred2* cassette and the endogenous *loxP* site in the BAC vector, we replaced the vector-derived *loxP* site with an I-SceI site using the same technology. The final BAC was purified with Nucleobond BAC 100 kit (Clontech) and co-injected with I-SceI into one-cell-stage zebrafish embryos. To generate *Tg (krtt1c19e:Venus-hGeminin)*$^{pd81}$ zebrafish, the basal keratinocyte promoter (*krtt1c19e*) (Lee et al., 2014) was subcloned upstream of Venus-hGeminin in the pSKS-1 vector (Sugiyama et al., 2009). The construct was then co-injected with I-SceI into one-cell-stage embryos.

For live imaging studies, animals were first anesthetized in aquarium water containing freshly diluted Tricaine (0.4 mg/ml; stock: 4 mg/ml) for 5–8 minutes until gill movements stopped. After imaging, gills were gently flushed with a plastic pipette until their movement resumed. Total amount of time in Tricaine was limited to less than 20 minutes. For studies of SEC homeostasis, adult female zebrafish at 4 to 8 months were used for imaging. For exfoliation injuries, a dry Kimwipe was gently pressed against the fin surface, and the extent of injury was immediately assessed under a Leica SP8 confocal microscope. To test effects

of various chemicals on SEC regeneration, SEC population on the fin epidermis was fully removed by exfoliation. Animals were then incubated in aquarium water containing either VAS2870 (0.5 μM; Sigma, SML0273), or $H_2O_2$ (0.5 μM; taken from a freshly opened bottle; BDH, BDH7690-1) for 48 hours before imaging. Animals were fed every day followed by a water change with fresh chemicals.

For fin amputation, 50% of caudal fins were removed with a razor blade. For wound closure studies, animals were anesthetized in aquarium water containing tricaine (0.2 mg/ml) or tricaine with 100 μM $Gd^{3+}$ (Sigma, G7532-5G) for 3 minutes before amputation. Animals were kept in the same solution during imaging acquisition, which began at 10 minutes post amputation. All images were captured from the center portion of the caudal fin (Area-1 in Figure S2A) except images shown in Figures 6 and 7. In Figure 6, images were captured from an area between the first and second rays on the lateral portion of the dorsal lobe (Area-4 in Figure S2A). In Figure 7, images were captured from interray areas, where basal cell responses were most consistent. All animal procedures were performed in accordance with Duke University guidelines.

## Imaging

Live imaging was performed using an upright Leica SP8 confocal microscope with a 25× water dipping lens (25×/0.95 HCXIRAPO WATER dipping lens 2.4 mm DIC). Only the 458 nm laser was used for imaging *skinbow* animals, which was sufficient to excite fluorescence in all three channels. Emission filters were established as following: Red channel, a filter with 585–620 nm band-pass. Green channel, a filter with 535–565 nm band-pass. Blue channel, a filter with 465–500 nm band-pass. Each channel was acquired simultaneously between lines. Images were recorded in 1024 × 1024 format (i.e. 465 μm × 465 μm). Scanning speed was set to 600 Hz in bidirectional mode. The zoom factor was set to 1, with the line average set to 2. Pinhole size was set to 2 AU. A z-stack of optical sections (every 1 or 2 μm) was acquired to cover the entire surface of the fin epithelium, which was ~30–70 μm in thickness for one side of the fin. The same imaging setting was used to image *skinbow; β-actin2:EGFP* animals, as cells labeled by β-*actin2:EGFP* line contain only one color in contrast to a mixed ratio of diverse colors in *skinbow*. For imaging two cell populations in *skinbow; krtt1c19e:Venus-hGeminin* animals, both 458 and 514 nm lasers were used. Emission filters were adjusted as following: Red, 585–600 nm; Green, 535–550 nm; Blue, 465–500 nm. CellRox Green Reagent (ThermoFisher, C10444) was used for detecting oxidative stress in the fin epithelium. Animals were anesthetized in aquarium water containing tricaine with the Cellrox dye (2.5 μM) for 5 minutes and then imaged in the same solution with the 488 nm laser and an emission spectrum of 500–540 nm.

## Image Analysis and Quantitative Analysis

*skinbow* raw confocal stacks from three channels were maximum-projected using LAS or Fiji. To increase the color diversity, we enhanced the contrast of each separate channel by equalizing its histogram, and assigned RGB Lookup tables for presentation. To correct for large-scale drift in low-time resolution (12 h) time-lapse movies or to generate single cell spatial trajectories, we employed Particle Image Velocimetry (PIV) techniques (Raffel et al., 1998). Briefly, a subimage centered on a set of either randomly chosen points or

corresponding to cell centroids is considered. For each subimage, the point of maximum cross-correlation is searched in a defined search window and is taken as the next point for trajectories or used to compute displacement. For image alignment, average displacement was subtracted to single cell displacements to correct for drift and/or movement occurring at scales larger than the field of view.

Single SEC areas and colors were obtained by semi-automatic tracking on time-lapse movies. Aligned time-lapse movies were used to manually identify cell gain or loss events, and cells were followed (forward or backward). Color distances were computed in the Lab space as normal Euclidean distances (Delta CIE 76). Color distance in Lab space was also used to compute image segmentation. Briefly, each channel was median-filtered to remove noise. Images were then transformed to Lab and filtered with a custom made filter that calculates the median of the color distance of the center pixel from a 5 × 5 pixel neighborhood (corresponding to a square of 2.25 um side). Resulting images were processed with Rotating Kernel filter (Lee and Rhodes, 1995) to enhance straight boundaries of given length and thickness (11 pixels and 3 pixels respectively, corresponding to roughly 5 and 1 um). Images were then processed by means of the Hessian-based Frangi Vesselness 2D Filter (Frangi et al., 1998) to identify all ridges and subsequently thresholded. Resulting segmentation was further corrected by eliminating segmented cells with extreme shape and size, and by eliminating those segmented cells corresponding to regions with too large color variance (i.e. corresponding to more than one color).

Cell gain and loss events were manually identified using aligned time-lapse movies. Spatial clustering of cell gain and loss was computed using Ripley's function (Bailey and Gatrell, 1995; Ripley, 1977). Briefly, for each cell death or loss events we measured the number of events in circular shells of increasing radii. This number is then divided by the average density. Randomly distributed points would result in a Ripley's K-function that is proportional to the area considered. Ripley's L-function is an adapted version of the K-function that allows deviations from complete spatial randomness to be mapped into deviations from zero. L-functions with positive values indicate clustering, while negative values would indicate regularity. L-function calculated for cell gain and loss events were compared with randomly distributed points with the same density as the experimental points, and with simulated clustered points. Clustered points were artificially generated by generating random 'seeding' points and then by adding points around seeding points to the desired density. To correct for edge effect, we used the toroidal correction method. Statistical significance was performed by testing values of L-function for each binned distance with a one-tailed t-test.

To reconstruct SECs trajectories in amputation assays with low-time resolution (12 h) we manually identified several corresponding cells in adjacent frames and reconstructed the spatial transformation mapping one set of points into the other. We then combined all of these consecutive transformations to reconstruct full trajectories, which were then used to calculate traveled distance, velocity and deformation.

To compute the number of distinguishable colors in *skinbow* images, we manually identified all visible cells in several images. We performed hierarchical clustering by color distance in

Lab space and imposed the maximum intra-cluster distance and the minimum a posteriori inter-cluster distance to be equal to the maximum color standard deviation in each cell. Image analysis was performed by means of custom-written MATLAB (The Mathworks) or Fiji scripts (Schindelin et al., 2012).

### Histological Assays

Frozen blocks were sectioned at 16 μm, mounted using Vectashield with DAPI, and examined by either fluorescence microscopy (Leica DM6000) or laser confocal microscopy (Zeiss 700). RNA in situ hybridization with caudal fins was performed as described (Poss et al., 2000), using digoxigenin-labeled probes to detect *CreER* expression.

## Supplementary Material

Refer to Web version on PubMed Central for supplementary material.

## Acknowledgments

We thank A. Dickson for artwork; J. Burris, N. Lee, T. Thoren, and T. Laffredo for zebrafish care; and M. Bagnat, B. Hogan, and T. Lechler for comments on the manuscript. B.D.C. was supported by a predoctoral fellowship from NSF. A.P. and L.P. are supported by Finalized Research and Founding for Investments in Basic Research (RBAP11BYNP-Newton). This work was supported by a grant from NIH (R01 GM074057) to K.D.P.

## References

Bailey, TC.; Gatrell, AC. Interactive spatial data analysis. Longman Scientific & Technical; 1995.

Barker N, van Es JH, Kuipers J, Kujala P, van den Born M, Cozijnsen M, Haegebarth A, Korving J, Begthel H, Peters PJ, et al. Identification of stem cells in small intestine and colon by marker gene Lgr5. Nature. 2007; 449:1003–1007. [PubMed: 17934449]

Bilan DS, Pase L, Joosen L, Gorokhovatsky AY, Ermakova YG, Gadella TW, Grabher C, Schultz C, Lukyanov S, Belousov VV. HyPer-3: a genetically encoded H(2)O(2) probe with improved performance for ratiometric and fluorescence lifetime imaging. ACS Chem Biol. 2013; 8:535–542. [PubMed: 23256573]

Blanpain C, Fuchs E. Epidermal homeostasis: a balancing act of stem cells in the skin. Nat Rev Mol Cell Biol. 2009; 10:207–217. [PubMed: 19209183]

Blanpain C, Fuchs E. Stem cell plasticity. Plasticity of epithelial stem cells in tissue regeneration. Science. 2014; 344:1242281. [PubMed: 24926024]

Clevers H. The intestinal crypt, a prototype stem cell compartment. Cell. 2013; 154:274–284. [PubMed: 23870119]

Discher DE, Janmey P, Wang YL. Tissue cells feel and respond to the stiffness of their substrate. Science. 2005; 310:1139–1143. [PubMed: 16293750]

Donati G, Watt Fiona M. Stem Cell Heterogeneity and Plasticity in Epithelia. Cell Stem Cell. 2015; 16:465–476. [PubMed: 25957902]

Doupe DP, Alcolea MP, Roshan A, Zhang G, Klein AM, Simons BD, Jones PH. A single progenitor population switches behavior to maintain and repair esophageal epithelium. Science. 2012; 337:1091–1093. [PubMed: 22821983]

Eisenhoffer GT, Loftus PD, Yoshigi M, Otsuna H, Chien CB, Morcos PA, Rosenblatt J. Crowding induces live cell extrusion to maintain homeostatic cell numbers in epithelia. Nature. 2012; 484:546–549. [PubMed: 22504183]

Elmore S. Apoptosis: a review of programmed cell death. Toxicol Pathol. 2007; 35:495–516. [PubMed: 17562483]

Frangi, A.; Niessen, W.; Vincken, K.; Viergever, M. Multiscale vessel enhancement filtering. In: Wells, W.; Colchester, A.; Delp, S., editors. Medical Image Computing and Computer-Assisted Intervention — MICCAI'98. Springer; Berlin Heidelberg: 1998. p. 130-137.

Gauron C, Rampon C, Bouzaffour M, Ipendey E, Teillon J, Volovitch M, Vriz S. Sustained production of ROS triggers compensatory proliferation and is required for regeneration to proceed. Sci Rep. 2013; 3:2084. [PubMed: 23803955]

Griffiths DF, Davies SJ, Williams D, Williams GT, Williams ED. Demonstration of somatic mutation and colonic crypt clonality by X-linked enzyme histochemistry. Nature. 1988; 333:461–463. [PubMed: 3374587]

Grove GL, Kligman AM. Age-associated changes in human epidermal cell renewal. J Gerontol. 1983; 38:137–142. [PubMed: 6827031]

Guillot C, Lecuit T. Mechanics of epithelial tissue homeostasis and morphogenesis. Science. 2013; 340:1185–1189. [PubMed: 23744939]

Gupta V, Poss KD. Clonally dominant cardiomyocytes direct heart morphogenesis. Nature. 2012; 484:479–484. [PubMed: 22538609]

Hunter GL, Crawford JM, Genkins JZ, Kiehart DP. Ion channels contribute to the regulation of cell sheet forces during Drosophila dorsal closure. Development. 2014; 141:325–334. [PubMed: 24306105]

Lechler T, Fuchs E. Asymmetric cell divisions promote stratification and differentiation of mammalian skin. Nature. 2005; 437:275–280. [PubMed: 16094321]

Lee RT, Asharani PV, Carney TJ. Basal keratinocytes contribute to all strata of the adult zebrafish epidermis. PLoS One. 2014; 9:e84858. [PubMed: 24400120]

Lee Y, Grill S, Sanchez A, Murphy-Ryan M, Poss KD. Fgf signaling instructs position-dependent growth rate during zebrafish fin regeneration. Development. 2005; 132:5173–5183. [PubMed: 16251209]

Lee YK, Rhodes WT. Rotating-kernel min-max algorithms for straight-line feature enhancement. Appl Opt. 1995; 34:290–298. [PubMed: 20963115]

Livet J, Weissman TA, Kang H, Draft RW, Lu J, Bennis RA, Sanes JR, Lichtman JW. Transgenic strategies for combinatorial expression of fluorescent proteins in the nervous system. Nature. 2007; 450:56–62. [PubMed: 17972876]

Love NR, Chen Y, Ishibashi S, Kritsiligkou P, Lea R, Koh Y, Gallop JL, Dorey K, Amaya E. Amputation-induced reactive oxygen species are required for successful Xenopus tadpole tail regeneration. Nat Cell Biol. 2013; 15:222–228. [PubMed: 23314862]

Macara IG, Guyer R, Richardson G, Huo Y, Ahmed SM. Epithelial homeostasis. Curr Biol. 2014; 24:R815825.

Mascre G, Dekoninck S, Drogat B, Youssef KK, Brohee S, Sotiropoulou PA, Simons BD, Blanpain C. Distinct contribution of stem and progenitor cells to epidermal maintenance. Nature. 2012; 489:257–262. [PubMed: 22940863]

Mugoni V, Camporeale A, Santoro MM. Analysis of oxidative stress in zebrafish embryos. J Vis Exp. 2014

Niethammer P, Grabher C, Look AT, Mitchison TJ. A tissue-scale gradient of hydrogen peroxide mediates rapid wound detection in zebrafish. Nature. 2009; 459:996–999. [PubMed: 19494811]

Poleo G, Brown CW, Laforest L, Akimenko MA. Cell proliferation and movement during early fin regeneration in zebrafish. Dev Dyn. 2001; 221:380–390. [PubMed: 11500975]

Poss KD. Advances in understanding tissue regenerative capacity and mechanisms in animals. Nat Rev Genet. 2010; 11:710–722. [PubMed: 20838411]

Poss KD, Shen J, Keating MT. Induction of lef1 during zebrafish fin regeneration. Dev Dyn. 2000; 219:282–286. [PubMed: 11002347]

Raffel, M.; Willert, CE.; Kompenhans, J. Particle Image Velocimetry: A Practical Guide ; with 24 Tables. Springer; 1998.

Rakers S, Niklasson L, Steinhagen D, Kruse C, Schauber J, Sundell K, Paus R. Antimicrobial peptides (AMPs) from fish epidermis: perspectives for investigative dermatology. J Invest Dermatol. 2013; 133:1140–1149. [PubMed: 23407389]

Ripley BD. Modelling spatial patterns. Journal of the Royal Statistical Society Series B (Methodological). 1977:172–212.

Ritsma L, Ellenbroek SI, Zomer A, Snippert HJ, de Sauvage FJ, Simons BD, Clevers H, van Rheenen J. Intestinal crypt homeostasis revealed at single-stem-cell level by in vivo live imaging. Nature. 2014; 507:362–365. [PubMed: 24531760]

Rompolas P, Deschene ER, Zito G, Gonzalez DG, Saotome I, Haberman AM, Greco V. Live imaging of stem cell and progeny behaviour in physiological hair-follicle regeneration. Nature. 2012; 487:496–499. [PubMed: 22763436]

Rompolas P, Mesa KR, Greco V. Spatial organization within a niche as a determinant of stem-cell fate. Nature. 2013; 502:513–518. [PubMed: 24097351]

Sakaue-Sawano A, Kurokawa H, Morimura T, Hanyu A, Hama H, Osawa H, Kashiwagi S, Fukami K, Miyata T, Miyoshi H, et al. Visualizing spatiotemporal dynamics of multicellular cell-cycle progression. Cell. 2008; 132:487–498. [PubMed: 18267078]

Santos-Ruiz L, Santamaria JA, Ruiz-Sanchez J, Becerra J. Cell proliferation during blastema formation in the regenerating teleost fin. Dev Dyn. 2002; 223:262–272. [PubMed: 11836790]

Schepeler T, Page ME, Jensen KB. Heterogeneity and plasticity of epidermal stem cells. Development. 2014; 141:2559–2567. [PubMed: 24961797]

Schindelin J, Arganda-Carreras I, Frise E, Kaynig V, Longair M, Pietzsch T, Preibisch S, Rueden C, Saalfeld S, Schmid B, et al. Fiji: an open-source platform for biological-image analysis. Nat Methods. 2012; 9:676–682. [PubMed: 22743772]

Shraiman BI. Mechanical feedback as a possible regulator of tissue growth. Proc Natl Acad Sci U S A. 2005; 102:3318–3323. [PubMed: 15728365]

Snippert HJ, van der Flier LG, Sato T, van Es JH, van den Born M, Kroon-Veenboer C, Barker N, Klein AM, van Rheenen J, Simons BD, et al. Intestinal crypt homeostasis results from neutral competition between symmetrically dividing Lgr5 stem cells. Cell. 2010; 143:134–144. [PubMed: 20887898]

Spallanzani, L.; Maty, M. An essay on animal reproductions. Becket, T.; de Hondt, PA., editors. 1769.

Sugiyama M, Sakaue-Sawano A, Iimura T, Fukami K, Kitaguchi T, Kawakami K, Okamoto H, Higashijima S, Miyawaki A. Illuminating cell-cycle progression in the developing zebrafish embryo. Proc Natl Acad Sci U S A. 2009; 106:20812–20817. [PubMed: 19923430]

ten Freyhaus H, Huntgeburth M, Wingler K, Schnitker J, Baumer AT, Vantler M, Bekhite MM, Wartenberg M, Sauer H, Rosenkranz S. Novel Nox inhibitor VAS2870 attenuates PDGF-dependent smooth muscle cell chemotaxis, but not proliferation. Cardiovasc Res. 2006; 71:331–341. [PubMed: 16545786]

Traver D, Paw BH, Poss KD, Penberthy WT, Lin S, Zon LI. Transplantation and in vivo imaging of multilineage engraftment in zebrafish bloodless mutants. Nat Immunol. 2003; 4:1238–1246. [PubMed: 14608381]

Watt FM. Mammalian skin cell biology: at the interface between laboratory and clinic. Science. 2014; 346:937–940. [PubMed: 25414300]

Wehner D, Weidinger G. Signaling networks organizing regenerative growth of the zebrafish fin. Trends Genet. 2015

Winton DJ, Ponder BA. Stem-cell organization in mouse small intestine. Proc Biol Sci. 1990; 241:13–18. [PubMed: 1978330]

Yang XC, Sachs F. Block of stretch-activated ion channels in Xenopus oocytes by gadolinium and calcium ions. Science. 1989; 243:1068–1071. [PubMed: 2466333]

## Highlights

- Transgenic *skinbow* zebrafish barcodes skin superficial epithelial cells (SECs)
- Hundreds of SECs are simultaneously monitored in vivo over cell surface lifetimes
- SEC behaviors quantified during regeneration of skin wounds or amputation injuries
- Identification and quantification of ROS effects on SEC regeneration

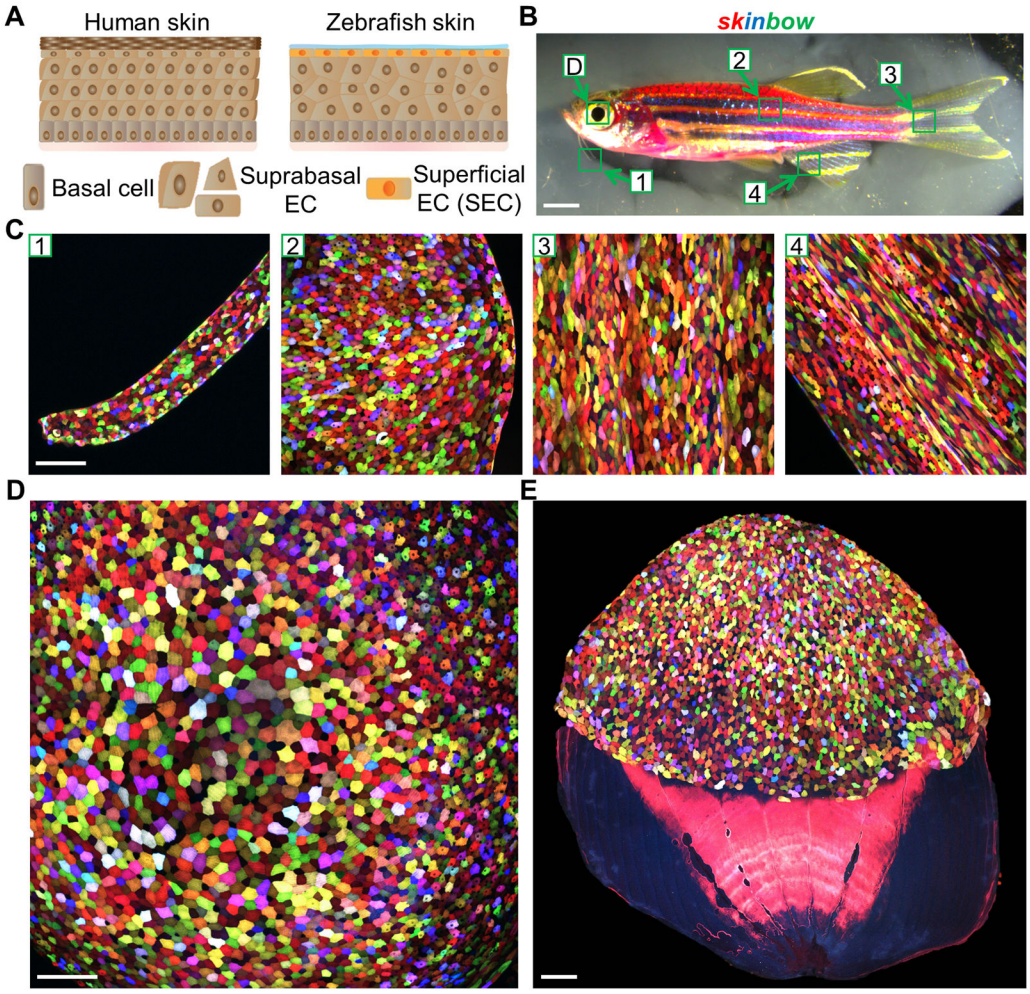


**Figure 1. Multicolor Labeling of Superficial Epithelial Cells (SECs) in *skinbow* Zebrafish**

(A) Schematic drawing of human and zebrafish skin. Zebrafish skin is a simple stratified epithelium without keratinized layers, with a surface covered by transparent mucus. EC, epithelial cell.

(B) Brightfield view of an adult *skinbow* animal. Green boxes indicate areas where the z-stacked confocal images shown in (C)(D) were captured. Scale bars, 2 mm.

(C) Multicolor labeling of skin epithelium in adult *skinbow* animals from areas shown in (B). Scale bars, 100μm.

(D and E) Multicolor labeling of corneal and scale epithelium in *skinbow*. A dissected scale is shown in (E). SECs cover the exposed portion of the scale (top). Scale bars, 100μm. See also Figure S1 and Movie S1.

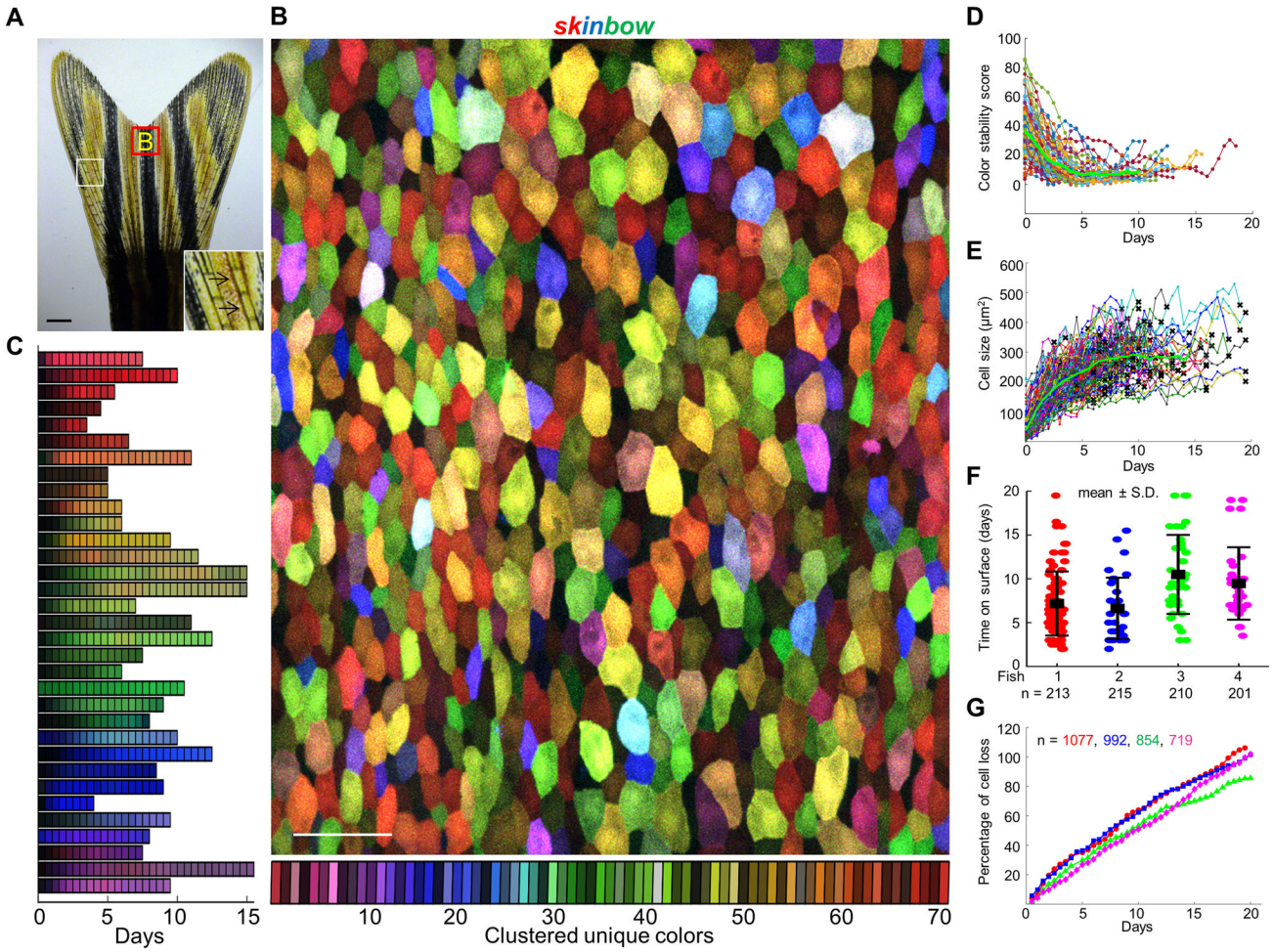


**Figure 2. Analysis of Epithelial Cell Turnover by Multicolor Labeling and Live Imaging**

(A) Brightfield view of adult zebrafish caudal fin. Inset depicts the alternating pattern of bony ray (black arrows) and interray tissues. Red box indicates areas where the z-stacked confocal images were captured. Scale bars, 1 mm.

(B) Multicolor labeling of adult fin epithelium. Superficial epithelial cells (SECs) on the fin surface label with one of ~70 unique colors (see Experimental Procedures for details). Scale bars, 50μm.

(C) Examples of SEC color dynamics during their presence on the fin surface. 33 representative cells are shown here, illustrating color stability over several days.

(D) Quantitative analysis showing color stability over time. The distance between the median color of each trajectory and its value at all times was calculated and aligned to their first appearance. Color distance is relatively high at early time points because of weak intensity upon first appearance, but stabilizes after the first 48 h. The green line represents the mean of trajectories (n = 87).

(E) Quantitative analysis indicating changes in SEC size over time. Single cell trajectories were aligned with respect to their first appearance on fin surface for comparison. Each line represents an independent trajectory with a black cross at the end indicating cell loss (n = 186 from 4 animals).

(F) Quantitative analysis showing average SEC lifespan under homeostatic conditions (n = 87, 32, 37, and 30 from 4 animals). Distribution of cell lifespan was measured as the duration of complete trajectories (from first appearance to loss). Bars indicate mean ± S.D. to indicate the spread of subjects.

(G) Large-scale surveillance of SEC loss over time. Percentage of cell loss events was plotted as sum of the missing cell number divided by total cell number at day 0 (n= 1077, 992, 854, and 719 from 4 animals), which could rise above 100% over an extended time period. See also Figures S2 and S3, and Movie S2.

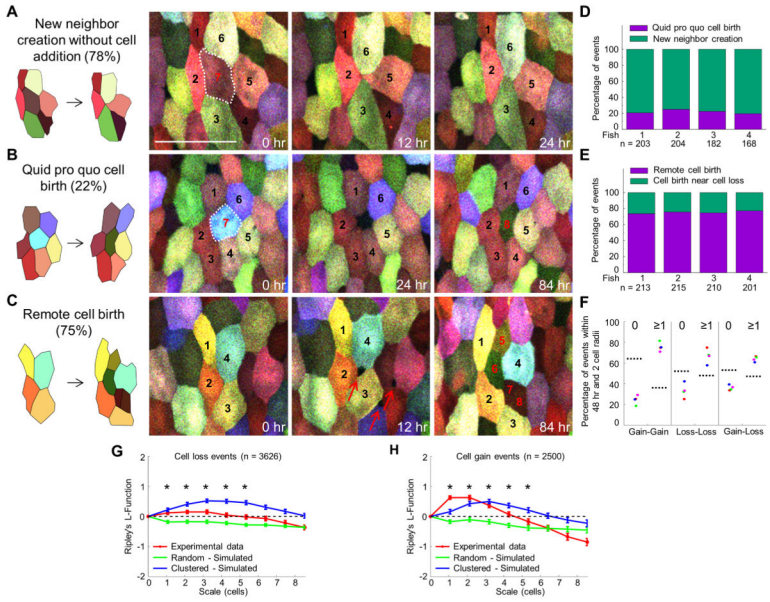


**Figure 3. Mechanisms of Cell Loss and Gain**

(A and B) Examples of time-lapse images indicating cell loss and gain events. White-dashed lines enclose SECs just prior to shedding (cells #7 in (A) and #7 in (B)). Events in (A) depict remodeling to generate new neighbors, whereas events in (B) depict a one-for-one cell replacement with cell #8 replacing cell #7.

(C) Example of time-lapse images depicting remote cell birth. Red arrows indicate pinhole openings for new SECs. Cells #5–8 in (C) are new SECs. Scale bar, 50 μm.

(D and E) Quantitative analyses of cell loss and gain events across 4 individuals.

(F) Analysis of spatiotemporal correlation between individual cell loss and gain events. The "Gain-Loss" category includes both Gain-Loss and Loss-Gain events. The plot shows the percentage of events that had no other events (or instead, at least one event) within a radius of 2 cell-lengths and within 48 h (24 h before and 24 h after). The results were compared to the corresponding case of randomly distributed points with the same density, as marked by dashed lines.

(G and H) Quantitative analyses of spatial distribution of cell loss and gain events. Ripley's L-function was used to assess deviation of spatial distribution of these two classes of events from that of randomly distributed points. A total of 3626 losses and 2500 gains events were collected in 41 time-points for each of the 4 animals analyzed. L-function greater than zero indicates clustering. Cell gain events are more clustered than cell loss events, as L is larger. Statistical significance was assessed by a one-tailed t-test for each point (experimental vs. simulated random). Bars indicate median ± S.E.M. Asterisks, $p < 0.05$. See also Figure S4.

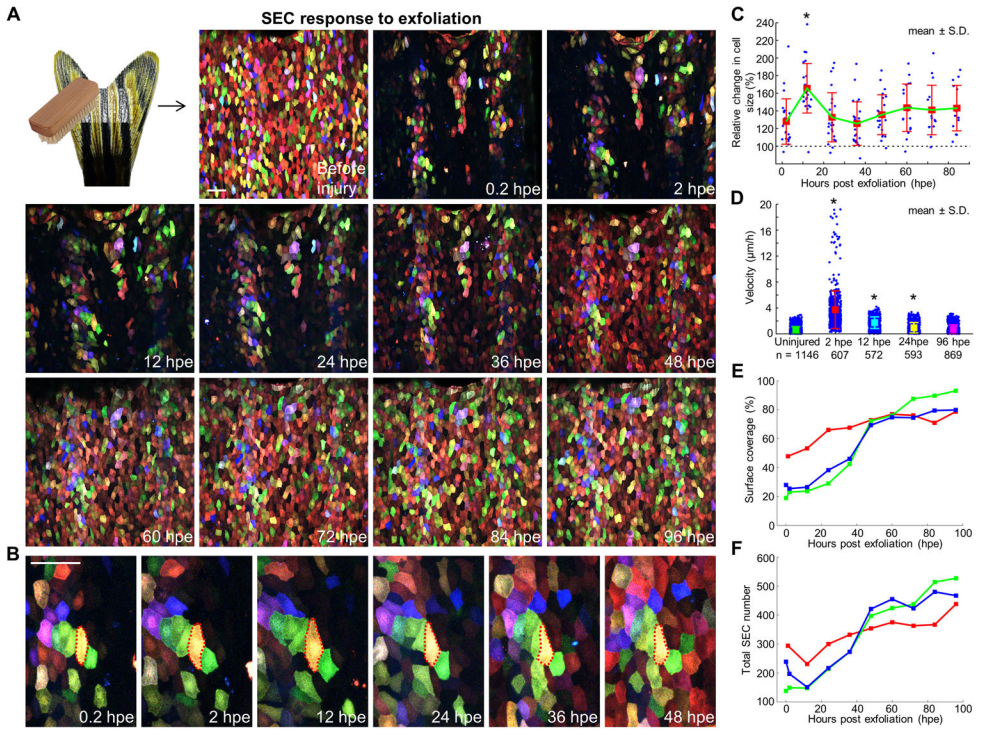


**Figure 4. Regeneration of Surface Injuries Involves a Biphasic Mechanism of Hypertrophy and Accelerated Replacement**

(A) (Top left) Schematic of exfoliation injury. (Images) A time lapse imaging series showing surface injuries and regeneration over a 4-day period. Scale bar, 50 μm.

(B) Enlarged view of a few cells during surface regeneration. Red dashed lines outline boundaries of a yellow cell undergoing transient hypertrophy. Scale bar, 50 μm.

(C) Quantification of relative change in SEC size after injury. The sizes of individual cells were normalized to their size immediately after injury, to indicate relative change (30% ± 5.4% greater at 2 hpe; 65.7 ± 5.9% greater at 12 hpe). Individual trajectories of spared SECs within the injured region were extracted from 3 independent scratch injuries (n = 20, 24, and 11). Bars indicate mean ± S.D. Statistical significance was assessed by a Mann-Whitney test (2 hpe vs. 12 hpe, $p < 10^{-4}$).

(D) Quantification of SEC velocities after injury. PIV type techniques were used to track single points in the images and compare typical velocities across adjacent timeframes. Uninjured SECs and those at 96 hours post scratch (hps) show similar velocities, while SECs are more motile immediately after injury. Values below the plot are the number of points (blue) used to build the plot. Bars indicate mean ± S.D. Statistical significance was assessed by a Mann-Whitney test (uninjured vs. 2 hpe, 12 hpe, or 24 hpe, $p < 10^{-5}$ for all cases).

(E) Quantification of change in surface coverage during regeneration (n = 3).

(F) Quantification of change in total SEC number during regeneration (n = 3). See also Movie S3.

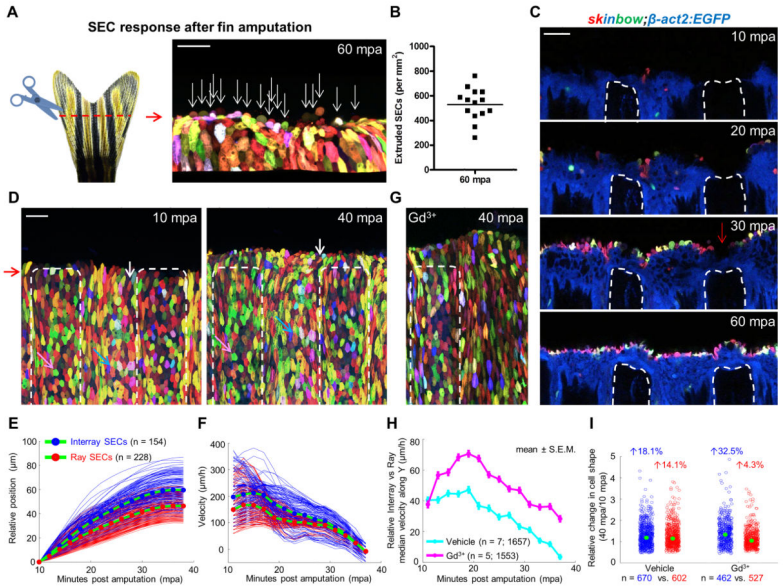


**Figure 5. Ray and Interray Epithelial Sheets Respond Distinctly to Amputation Injury**

(A) (Left) Schematic of fin amputation. (Right) Confocal image indicating extruded SECs at the amputation plane by 60 minutes post amputation (mpa). A three-dimensional image was reconstructed from z-stacks of confocal images, using Imaris to facilitate counting of extruded cells. White arrows point to extruded cells along the amputation plane. Scale bar, 50 µm.

(B) Quantification of extruded SECs at the injury site at 60 minutes post amputation (n = 14 regions from 7 animals).

(C) Time lapse images of optical sections at the same z-position post amputation. Images were captured every 10 minutes starting at 10 minutes post amputation. White dashed lines outline fin rays. Red arrow indicates that the fin ray stump is covered first by basal and suprabasal cells, closed trailed by SECs. Scale bar, 50 µm.

(D) Confocal images captured at 10 and 40 mpa. White dashed lines outline regions covering fin rays. Images were recorded every 2 minutes for 30 minutes starting at 10 mpa. White, pink, and blue arrows point to individual cells at 10 and 40 mpa. Scale bar, 50 µm.

(E) Position of single cells perpendicular to the amputation plane with respect to starting position. Average trajectories are plotted in green lines with blue (interray SECs) and red (ray SECs) filled circles.

(F) Velocities were obtained by single cell tracking as finite differences.

(G) A confocal image captured at 40 mpa from animals treated with gadolinium ($Gd^{3+}$). White dashed lines outline regions covering fin rays.

(H) Relative velocity of interray with respect to ray SECs in vehicle- (cyan, n = 7) vs $Gd^{3+}$-treated animals (magenta, n = 5) averaged over all trajectories first and then over different samples. Data are plotted as mean ± S.E.M. $Gd^{3+}$ treatment increases differential migration rates of interray SECs with respect to ray SECs. Additionally, migration persists in $Gd^{3+}$-treated animals beyond 40 min.

(I) Quantification of relative changes in cell shape for interray SECs (blue) and ray SECs (red) in either vehicle- or $Gd^{3+}$-treated animals. Cell shape was determined by aspect ratio,

which was obtained as the major to minor axis ratio for each cell. The aspect ratio of individual cells at 40 mpa was normalized to the average value at 10 mpa to show relative change. Total numbers of analyzed trajectories are indicated below each point cloud, combined from 7 (vehicle) and 5 ($Gd^{3+}$) animals. Mann-Whitney test of vehicle vs. $Gd^{3+}$ interray SECs (blue circles) yielded a significant difference in the medians (green dots) of the two samples ($p = 0.0038$). See also Figure S5, and Movies S4, S5 and S6.

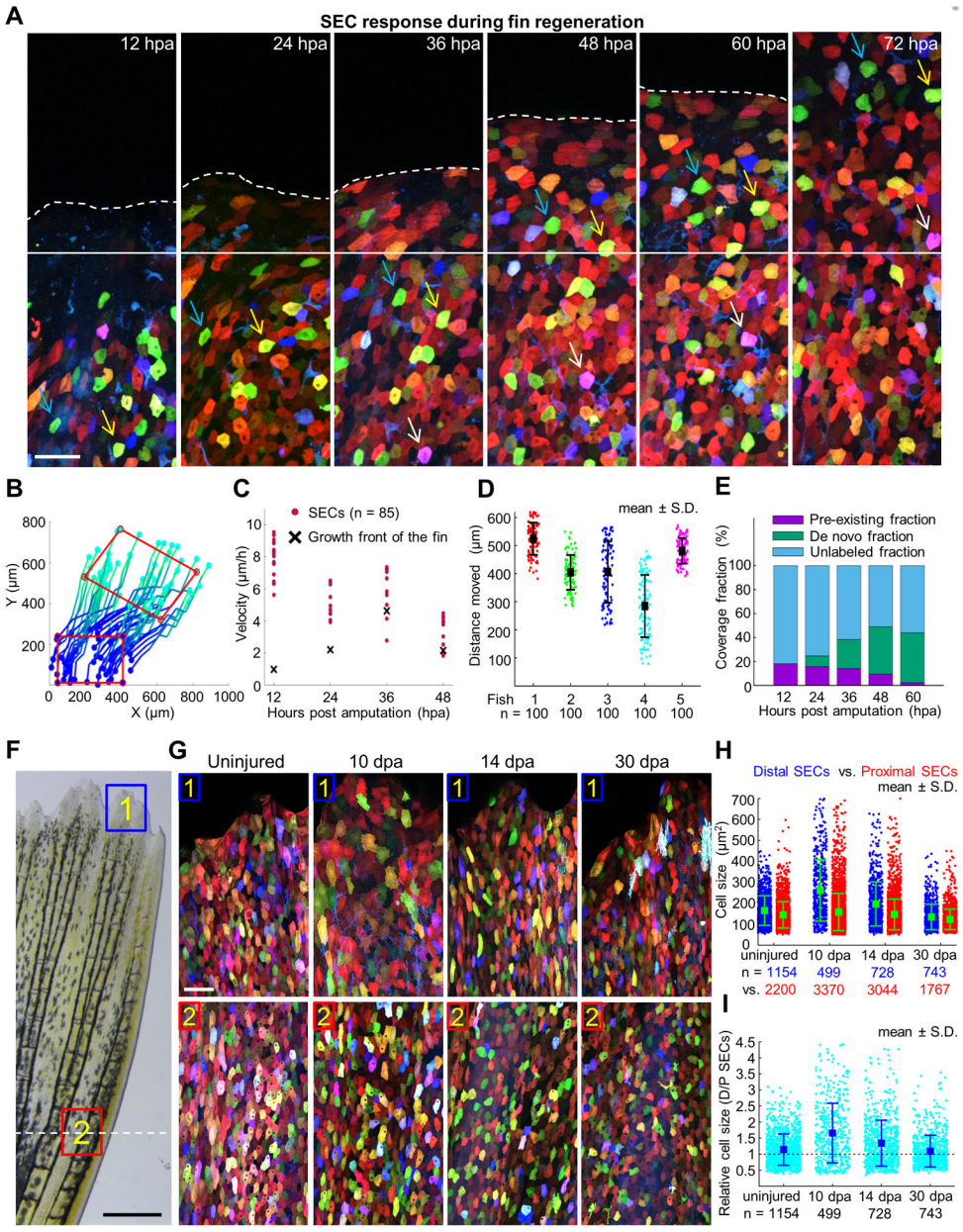


**Figure 6. Acquisition of Surface Epithelium from Pre-Existing and *De Novo* Pools during Fin Regeneration**

(A) Time lapse images of an amputated *skinbow* fin during regeneration. Images were captured once each 12 hours over a 4-day period. Solid white line marks the growth front. White dashed line indicates the amputation plane. Blue, yellow, and white arrows point to individual cells across consecutive imaging times. Scale bars, 50 μm.

(B) Reconstruction of trajectories from one representative animal. Each line here represents a reconstructed trajectory of a migratory cell. Color codes for time (i.e. dark blue is the beginning of each trajectories, 12 hpa, and cyan is the end, 96 hpa). To better visualize the movement of cells within the epidermis, a red rectangle indicates positions in the initial and final frames. The rectangle is translocated and deformed, revealing both cell migration and

deformation of the tissue. Rightward movement of the cells likely reflects the stereotypical growth pattern of the lateral portion of the dorsal lobe, from which images were captured.
(C) Quantification of velocities of individual cells (red dots; n = 85). The velocity of the moving growth front is marked with a black cross.
(D) Quantitative analysis of average SEC distances traveled between 12 and 96 hpa. 100 reconstructed trajectories each from five animals were considered. Bars indicate mean ± S.D.
(E) Quantitative analysis representing SEC contribution from de novo creation versus that generated by migration of SECs identified at 12 hpa. We tracked the region, initially located proximal to the amputation plane at 12 hpa, by reconstructing cell movements at large-scale (Figure S6B). The extent of unlabeled regions, of SECs already present at 12 hpa (pre-existing fraction), and of SECs that appear over the course of the experiment (de novo fraction) is quantified at each time. The contribution of newly added SECs was calculated as the difference between the labeled and pre-existing fractions.
(F) Brightfield view of a fin at 10 dpa. Scale bars, 0.5 mm. Blue and red boxes indicate areas where z-stacked confocal images in (G) were captured. White-dashed line indicates the amputation plane.
(G) Images of *skinbow* SECs from distal (#1) and proximal (#2) regions of the same fin for each individual at 10, 14, and 30 dpa. At 10 dpa, distal SECs are visibly larger than proximal SECs. Scale bars, 50 μm.
(H) Quantification of cell size for proximal (red) and distal SECs (blue) in regenerating fins (n = 5 animals for each time). Total numbers of analyzed cells are indicated below each point cloud. Bars indicate mean ± S.D. Statistical significance between proximal and distal SEC cell sizes in 10 dpa and 14 dpa samples was assessed by a one-tailed t-test, $p < 10^{-5}$. Cell sizes indicate sampled population averages of cells at all stages of surface life, from fins that would not display any effects of repetitive imaging.
(I) Quantification of fold change in cell size for proximal (red) and distal SECs (blue) in regenerating fins. Total numbers of analyzed cells are indicated below each point cloud. Bars indicate mean ± S.D. The cell size ratio (distal SECs/proximal SECs) steadily decreases from 1.65 ± 0.04 (10 dpa), to 1.34 ± 0.03 (14 dpa), to 1.09 ± 0.03 (30 dpa). Uninjured fins have a ratio of 1.14 ± 0.01. See also Figure S7.

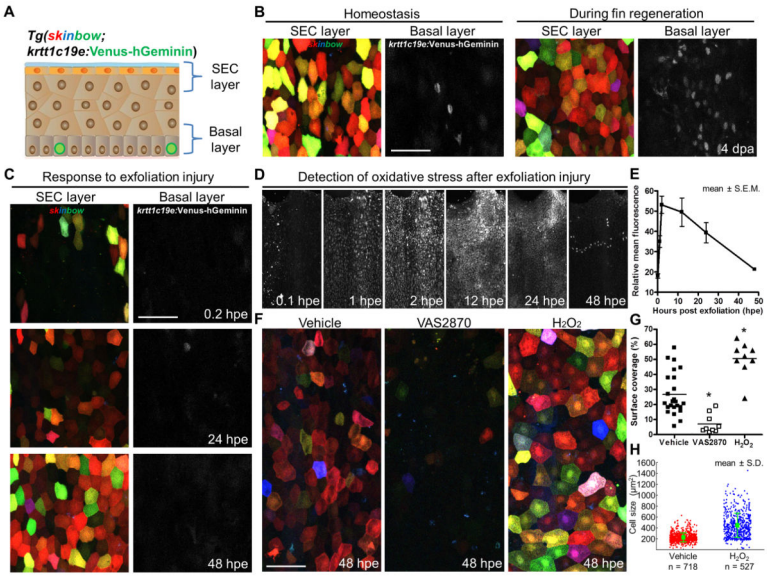


**Figure 7. SEC Regeneration After Exfoliation Is Regulated by Injury-Induced ROS**

(A) Schematic of cell layers that are labeled in *skinbow; krtt1c19e:Venus-hGeminin* skin.

(B) Images of SECs and cycling basal progenitor cells (grayscale) under homeostatic conditions (left) and 4 days following fin amputation (right), indicating intense basal cell proliferation during fin regeneration. Images of SEC and basal layers were maximum-projected from respective z-positions. Scale bar, 50 μm.

(C) A time lapse imaging series showing SEC regeneration after exfoliation, indicating minimal basal progenitor cell cycle entry. Scale bar, 50 μm.

(D) A time lapse imaging series displaying transient ROS presence in the fin epithelium after exfoliation. ROS were indirectly detected as oxidative stress *in vivo* using Cellrox, a cell-permeable fluorescent probe.

(E) Quantification of the relative change in fluorescence intensity after exfoliation from experiments in (D). Data are plotted as mean ± S.E.M (n = 6 animals).

(F) Representative images of fin SECs at 48 hpe after various treatments. Animals were continuously treated in chemicals that either inhibit (VAS2870) or enhance ($H_2O_2$) ROS presence after injury.

(G) Quantification of surface coverage in the fin epithelium at 48 hpe. Horizontal Bars indicate mean in each group (n = 9 to 24 animals). Statistical significance between vehicle and treated groups was assessed by a two-tailed t-test (vehicle vs. VAS2870, or $H_2O_2$; $p < 10^{-3}$ for both cases).

(H) Quantification of SEC size in the fin epithelium at 48 hpe. Quantification of cell size for vehicle (red) and $H_2O_2$ (blue) treated animals (n = 8 vs. 5 animals). Total numbers of analyzed cells are indicated below each point cloud. Bars indicate mean ± S.D. Statistical significance between the vehicle and $H_2O_2$ groups was assessed by a two-tailed t-test, $p < 10^{-4}$ for either collapsing all single cell data together or using the means of different animals. The vehicle group has cell size of 212.50 ± 3.09 $\mu m^2$, vs. 411.36 ± 9.70 in the $H_2O_2$-treated group. See also Movie S7.